the rate (the smaller the rate, the larger the gain), the encoding complexity (the greater the complexity, the greater the gain), and the degree of inter-pixel correlation (the greater the correlation, the greater the gain). Standard coding algorithms such as JPEG and JPEG-LS perform much better than GPCM at the expense of a significantly larger computational complexity.

ACKNOWLEDGMENT

The authors would like to thank S.-G. Park and A. Roca for helpful discussions.

REFERENCES

[1] N. S. Jayant and P. Noll, *Digital Coding of Waveforms*. Englewood Cliffs, NJ: Prentice-Hall, 1984.

[2] Z. Xiong, A. Liveris, and S. Cheng, "Distributed source coding for sensor networks," *IEEE Signal Process. Mag.*, vol. 21, no. 5, pp. 80–94, Sep. 2004.

[3] H. Shum and T. Komura, "Tracking the translational and rotational movement of the ball using high-speed camera movies," in *Proc. IEEE Int. Conf. Image Process.*, Genoa, Italy, Sep. 2005, pp. 1084–1087.

[4] J. Sekikawa and T. Kubono, "Spectroscopic imaging observation of break arcs using a high-speed camera," in *Proc. IEEE Conf. Electr. Contacts*, Sep. 2007, pp. 275–279.

[5] P. Gemeiner, W. Ponweiser, P. Einramhof, and M. Vincze, "Real-time SLAM with high-speed CMOS camera," in *Proc. IEEE Int. Conf. Imag. Anal. Process.*, Sep. 2007, pp. 297–302.

[6] M. El-Desouki, M. J. Deen, Q. Fang, L. Liu, F. Tse, and D. Armstrong, "CMOS image sensors for high speed applications," *Sensors*, vol. 9, no. 1, pp. 430–444, 2009.

[7] T. H. Khan and K. A. Wahid, "Low power and low complexity compressor for video capsule endoscopy," *IEEE Trans. Circuits Syst. Video Technol.*, vol. 21, no. 10, pp. 1534–1546, Oct. 2011.

[8] A. N. Kim, T. A. Ramstad, and I. Balasingham, "Very low complexity low rate image coding for the wireless endoscope," in *Proc. Int. Symp. Appl. Sci. Biomed. Commun. Technol.*, Barcelona, Spain, Oct. 2011, pp. 90-1–90-5.

[9] M. J. Weinberger, G. Seroussi, and G. Sapiro, "The LOCO-I lossless image compression algorithm: Principles and standardization into JPEG-LS," *IEEE Trans. Image Process.*, vol. 9, no. 8, pp. 1309–1324, Aug. 2000.

[10] J. Prades Nebot, A. Roca, and E. Delp, "Modulo-PCM based encoding for high speed video cameras," in *Proc. IEEE Int. Conf. Imag. Process.*, San Diego, CA, Oct. 2008, pp. 153–156.

[11] J. Prades Nebot, "Very low-complexity coding of images using adaptive Modulo-PCM," in *Proc. IEEE Int. Conf. Imag. Process.*, Brussels, Belgium, Sep. 2011, pp. 313–316.

[12] N.-M. Cheung, H. Wang, and A. Ortega, "Sampling-based correlation estimation for distributed source coding under rate and complexity constraints," *IEEE Trans. Image Process.*, vol. 17, no. 11, pp. 2122–2137, Nov. 2008.

[13] T. M. Cover and J. A. Thomas, *Elements of Information Theory*. New York: Wiley, 1991.

[14] G. Wolberg, *Digital Image Warping*. New York: Wiley, 1990.

[15] B. Zeng and A. Venetsanopoulos, "A JPEG-based interpolative image coding scheme," in *Proc. IEEE Int. Conf. Acoust. Speech Signal Process.*, Minneapolis, MN, Apr. 1993, pp. 393–396.

[16] M. Morbee, "Optimized information processing in resource-constrained vision systems: From low-complexity coding to smart sensor networks," Ph.D. dissertation, Faculty Eng. Archit., Ghent Univ., Ghent, Belgium, Mar. 2011.

[17] E. Cho, M. J. Cho, and J. Eltinge, "The variance of sample variance from a finite population," *Int. J. Pure Appl. Math.*, vol. 21, pp. 387–394, May 2005.

[18] A. K. Jain, *Fundamentals of Digital Image Processing*. Englewood Cliffs, NJ: Prentice-Hall, 1989.

[19] E. Feig and S. Winograd, "Fast algorithms for the discrete cosine transform," *IEEE Trans. Signal Process.*, vol. 40, no. 9, pp. 2174–2193, Sep. 1992.

Weighted Similarity-Invariant Linear Algorithm for Camera Calibration With Rotating 1-D Objects

Kunfeng Shi, Qiulei Dong, and Fuchao Wu

***Abstract*— In this paper, a weighted similarity-invariant linear algorithm for camera calibration with rotating 1-D objects is proposed. First, we propose a new estimation method for computing the relative depth of the free endpoint on the 1-D object and prove its robustness against noise compared with those used in previous literature. The introduced estimator is invariant to image similarity transforms, resulting in a similarity-invariant linear calibration algorithm which is slightly more accurate than the well-known normalized linear algorithm. Then, we use the reciprocals of the standard deviations of the estimated relative depths from different images as the weights on the constraint equations of the similarity-invariant linear calibration algorithm, and propose a weighted similarity-invariant linear calibration algorithm with higher accuracy. Experimental results on synthetic data as well as on real image data show the effectiveness of our proposed algorithm.**

***Index Terms*— 1-D calibration object, camera calibration, weighted similarity-invariant linear algorithm (WSILA).**

I. INTRODUCTION

One-dimensional calibration techniques are an important type of techniques that generally use a stick consisting of at least three points to calibrate camera parameters [1]–[11]. Since the 1-D object can be observed without occlusion by all the referred cameras simultaneously, 1-D calibration techniques are more applicable in multicamera systems [12], [13] than 2-D and 3-D calibration techniques [14]–[16].

In recent years, 1-D calibration techniques have been studied extensively. Zhang [1] for the first time proposed a linear calibration algorithm using a 1-D object that rotated around a fixed point. Hammarstedt *et al*. [3] investigated in detail the degenerate configurations of [1]. Wu *et al*. [2] reformulated the calibration equation of [1] in a geometric method and obtained a linear algorithm with similar accuracy. Francca *et al*. [6] proposed a linear algorithm with the normalized image points, which significantly improved the calibration accuracy of [1]. To avoid possible nonpositive-definite estimations of the image of absolute conic (IAC) in the linear calibration algorithms, Wang *et al*. [7] minimized the norm of algebraic residuals subject to the constraint that the solution was positive definite. Miyagawa *et al*. [8] calibrated the camera's focal length from a single image of two orthogonal 1-D objects that shared one point. In addition, when multiple cameras need to be globally calibrated, single-camera calibration algorithms can be extended by combining the intrinsic and extrinsic parameters of all the cameras. Moreover, Wang *et al*. [9] showed that multiple cameras can be simultaneously calibrated with a 1-D object that underwent general rigid motions.

Manuscript received August 26, 2011; revised January 18, 2012; accepted March 26, 2012. Date of publication April 17, 2012; date of current version July 18, 2012. This work was supported in part by the National Natural Science Foundation of China under Grant 60835003 and Grant 60905020. The associate editor coordinating the review of this manuscript and approving it for publication was Dr. Adrian G. Bors.

The authors are with the National Laboratory of Pattern Recognition, Institute of Automation, Chinese Academy of Sciences, Beijing 100190, China (e-mail: kfshi@nlpr.ia.ac.cn; qldong@nlpr.ia.ac.cn; fcwu@nlpr.ia.ac.cn).

Color versions of one or more of the figures in this paper are available online at http://ieeexplore.ieee.org.

Digital Object Identifier 10.1109/TIP.2012.2195013

This paper focuses on how to improve the accuracies of linear calibration techniques with rotating 1-D objects. The calibration principle of [2] is different from that of [1] and [6], and the accuracy of [2] is similar to that of [1]. Therefore, the linear algorithms in [1] and [6] are discussed in detail in this paper. To improve the calibration robustness against the measurement errors of image points, we first introduce a new algorithm for computing the relative depths of the free endpoints, and compare it with two existing algorithms [1], [6]. Then, we analyze the influence of data normalization on the calibration accuracy and give a new explanation on why the performance of [6] is superior to that of [1]. Finally, based on the introduced algorithm for computing the relative depths, we propose a weighed similarity-invariant linear calibration algorithm that uses the reciprocals of the standard deviations of the computed relative depths to weight the constraint equations.

The remainder of this paper is organized as follows. Section II describes related work. Section III introduces a new relative depth computation algorithm and compares it with existing algorithms. We propose a weighted similarity-invariant linear calibration algorithm in Section IV. Section V reports experimental results, followed by some concluding remarks in Section VI.

II. Related Work

A. Preliminaries

Here, an image point is denoted by $\mathbf{x} = [u, v]^\top$, and its homogeneous coordinate is $\widetilde{\mathbf{x}} = [u, v, 1]^\top$. A space point is denoted by $\mathbf{X} = [X, Y, Z]^\top$. The weighted norm of a vector $\mathbf{v}$ is $\|\mathbf{v}\|_{\mathtt{M}} = \sqrt{\mathbf{v}^\top \mathtt{M}\mathbf{v}}$, where $\mathtt{M}$ is a positive definite matrix. And we define $\mathtt{I}_{m\times n}$ as an $m\times n$ matrix with 1s on the diagonal and 0s elsewhere. Throughout this paper, we use typewriter font for matrices, boldface font for vectors, and Italic font for scalar quantities.

Fig. 1 is an illustration of a 1-D calibration object consisting of three collinear points. The point $\mathbf{X}_1$ is fixed while the 1-D object rotates around it. The number of the 1-D object's poses is denoted by I, and the number of the points on it is denoted by J. $\mathbf{X}_j^i$ ($i = 1, 2, \ldots, I$ and $j = 2, \ldots, J$) denotes the position of the point j in the pose i, and the spatial distance between $\mathbf{X}_1$ and $\mathbf{X}_j^i$ is L_j. The calibration matrix of a pinhole camera is

$$\mathtt{K} = \begin{bmatrix} f_u & \gamma & u_0 \\ 0 & f_v & v_0 \\ 0 & 0 & 1 \end{bmatrix} \tag{1}$$

where $[f_u, f_v]$ is the focal length, γ is the skew factor, and $[u_0, v_0]^\top$ is the principal point. Under the camera coordinate frame, the space points and their image coordinates satisfy

$$\mathbf{X}_1 = Z_1\mathtt{K}^{-1}\widetilde{\mathbf{x}}_1, \mathbf{X}_2^i = Z_2^i\mathtt{K}^{-1}\widetilde{\mathbf{x}}_2^i, \ldots, \mathbf{X}_J^i = Z_J^i\mathtt{K}^{-1}\widetilde{\mathbf{x}}_J^i. \tag{2}$$

The relative depth of the free endpoint $\mathbf{X}_J^i$ is the ratio of its depth to the depth of the fixed point $\mathbf{X}_1$, denoted by $\beta_i = Z_J^i/Z_1$. Different methods to compute $\widehat{\beta}_i$ result in different linear calibration algorithms.

B. Zhang's Linear Algorithm (ZLA)

ZLA [1] consists of two steps: estimating the relative depths and establishing a set of linear constraints on the IAC. When $J = 3$, the relative depth β_i is estimated as

$$\widehat{\beta}_i^{(1)} = \frac{(L_3 - L_2)(\widetilde{\mathbf{x}}_1 \times \widetilde{\mathbf{x}}_2^i)^\top(\widetilde{\mathbf{x}}_2^i \times \widetilde{\mathbf{x}}_3^i)}{L_2\|\widetilde{\mathbf{x}}_2^i \times \widetilde{\mathbf{x}}_3^i\|^2}. \tag{3}$$

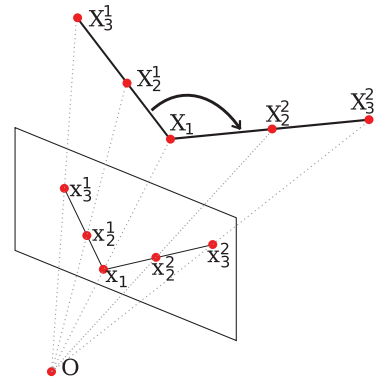

Fig. 1. Illustration of a rotating 1-D calibration object.

Since $\|\mathbf{X}_1 - \mathbf{X}_3^i\|^2 = L_3^2$ ($i = 1, 2, \ldots, I$), a constraint on $\omega = Z_1{}^2\mathtt{K}^{-\top}\mathtt{K}^{-1}$ can be obtained from the image of the pose i according to (2) as follows:

$$\left(\widetilde{\mathbf{x}}_1 - \widehat{\beta}_i^{(1)}\widetilde{\mathbf{x}}_3^i\right)^\top \omega\left(\widetilde{\mathbf{x}}_1 - \widehat{\beta}_i^{(1)}\widetilde{\mathbf{x}}_3^i\right) = L_3^2. \tag{4}$$

Let $\mathbf{w} = [\omega_{11}, \omega_{12}, \omega_{22}, \omega_{13}, \omega_{23}, \omega_{33}]^\top$, and then (4) is converted to a linear constraint on $\mathbf{w}$ as $\boldsymbol{\xi}_i^\top\mathbf{w} = L_3^2$, where $\boldsymbol{\xi}_i$ is the coefficient vector of $\mathbf{w}$ in (4). Combining constraints on $\mathbf{w}$ from I images, a linear system of equations results, given by

$$\mathtt{V}\mathbf{w} = \mathbf{L}. \tag{5}$$

Once at least six images are captured without motion singularity, $\mathbf{w}$ can be determined uniquely as $\widehat{\mathbf{w}} = \mathtt{V}^+\mathbf{L}$. Then, $\widehat{\omega}$ and $\widehat{\mathtt{K}}$ can be computed.

C. Francca et al.'s Normalized Linear Algorithm (FNLA)

To decrease the influence of image noise on ZLA, Francca *et al.* [6] used the normalized image points to calibrate the camera as follows. Denote the image normalization matrix by $\mathtt{H}$, and the normalized image points are $\widetilde{\mathbf{x}}_1' = \mathtt{H}\widetilde{\mathbf{x}}_1, \widetilde{\mathbf{x}}_j^{i\prime} = \mathtt{H}\widetilde{\mathbf{x}}_j^i$, ($i = 1, 2, \ldots, I$, $j = 2, 3, \ldots, J$). With $\widetilde{\mathbf{x}}_1'$, $\widetilde{\mathbf{x}}_j^{i\prime}$, and $\widetilde{\mathbf{x}}_J^{i\prime}$, β_i is estimated as

$$\widehat{\beta}_{ij}^{(2)} = \frac{(L_J - L_j)\left(\widetilde{\mathbf{x}}_1' \times \widetilde{\mathbf{x}}_j^{i\prime}\right)^\top\left(\widetilde{\mathbf{x}}_j^{i\prime} \times \widetilde{\mathbf{x}}_J^{i\prime}\right)}{L_j\left\|\widetilde{\mathbf{x}}_j^{i\prime} \times \widetilde{\mathbf{x}}_J^{i\prime}\right\|^2}, \quad j = 2, 3, \ldots, J-1. \tag{6}$$

Define the normalized IAC as $\omega' = \mathtt{H}^{-\top}\omega\mathtt{H}^{-1}$, and then the constraint on ω' is

$$\left(\widetilde{\mathbf{x}}_1' - \widehat{\beta}_{ij}^{(2)}\widetilde{\mathbf{x}}_J^{i\prime}\right)^\top \omega'\left(\widetilde{\mathbf{x}}_1' - \widehat{\beta}_{ij}^{(2)}\widetilde{\mathbf{x}}_J^{i\prime}\right) = L_J^2. \tag{7}$$

Similar to (5), from the $I(J-2)$ constraints in (7), a linear system of equations on $\mathbf{w}' = \left[\omega_{11}', \omega_{12}', \omega_{22}', \omega_{13}', \omega_{23}', \omega_{33}'\right]^\top$ is given by

$$\mathtt{V}'\mathbf{w}' = \mathbf{L}. \tag{8}$$

After computing $\mathbf{w}'$ and $\widehat{\omega}'$, the calibration matrix $\widehat{\mathtt{K}}$ is obtained from $\widehat{\omega} = \mathtt{H}^\top\widehat{\omega}'\mathtt{H}$.

D. Maximum-Likelihood Estimation of the Pinhole Camera Model (MLEPCM)

Zhang [1] and Francca *et al.* [6] also used nonlinear optimization to refine their linear calibration results. Suppose the variance of

the noise on image point $\mathbf{x}_j^i$ is $\Sigma_{\mathbf{x}_j^i}$, and then the maximum-likelihood estimation of the pinhole camera model can be computed by minimizing the reprojection error

$$\left\|\mathbf{x}_1-\widehat{\mathbf{x}}_1(\widehat{\mathtt{K}},\widehat{\mathbf{X}}_1)\right\|^2_{\Sigma_{\mathbf{x}_1}^{-1}}+\sum_{i=1}^{I}\sum_{j=2}^{J}\left\|\mathbf{x}_j^i-\widehat{\mathbf{x}}_j^i(\widehat{\mathtt{K}},\widehat{\mathbf{X}}_j^i)\right\|^2_{\Sigma_{\mathbf{x}_j^i}^{-1}} \tag{9}$$

where $\widehat{\mathbf{x}}_j^i$ is the estimated projection of $\widehat{\mathbf{X}}_j^i$ according to (2), and $\widehat{\mathbf{X}}_j^i=\widehat{\mathbf{X}}_1+L_j[\sin\theta_i\cos\phi_i,\sin\theta_i\sin\phi_i,\cos\theta_i]^\top$, where (θ_i,ϕ_i) are the spherical coordinates at the pose i.

III. New Algorithm for Relative Depth Computation

In this section, we first introduce a new algorithm to estimate the relative depth of the free endpoint at each pose of the 1-D object. Then, the detailed analyses of the accuracies of different relative depth computation algorithms are given. The influence of data normalization on the calibration accuracy is also revisited.

A. Similarity-Invariant Algorithm for Computing the Relative Depths

From the collinearity of $\mathbf{X}_1$, $\mathbf{X}_j^i$, and $\mathbf{X}_J^i$, we obtain $(\mathbf{X}_J^i-\mathbf{X}_1)/L_J=(\mathbf{X}_j^i-\mathbf{X}_1)/L_j$, and then

$$L_J\mathbf{X}_j^i=(L_J-L_j)\mathbf{X}_1+L_j\mathbf{X}_J^i. \tag{10}$$

By substituting (2) into (10) and eliminating $\mathtt{K}^{-1}$ from both sides, we have

$$L_JZ_j^i\widetilde{\mathbf{x}}_j^i=(L_J-L_j)Z_1\widetilde{\mathbf{x}}_1+L_jZ_J^i\widetilde{\mathbf{x}}_J^i. \tag{11}$$

Equation (11) can provide three linear equations in Z_1, Z_j^i, and Z_J^i. After eliminating Z_j^i by substitution and dividing both sides of (11) by Z_1, the linear constraints on β_i are given by

$$L_j(\mathbf{x}_j^i-\mathbf{x}_J^i)\beta_i=(L_J-L_j)(\mathbf{x}_1-\mathbf{x}_j^i),\quad j=2,\ldots,J-1. \tag{12}$$

The $2(J-2)$ constraints in (12) form a linear system of equations, and the least-squares solution is

$$\widehat{\beta}_i^{(3)}=\frac{\sum_{j=2}^{J-1}\left[L_j(L_J-L_j)(\mathbf{x}_1-\mathbf{x}_j^i)^\top(\mathbf{x}_j^i-\mathbf{x}_J^i)\right]}{\sum_{j=2}^{J-1}\left[L_j^2\|\mathbf{x}_j^i-\mathbf{x}_J^i\|^2\right]}. \tag{13}$$

Since similarity transform (isotropic normalization) preserves the ratio between vector inner products, $\widehat{\beta}_i^{(3)}$ is similarity-invariant regardless of the noises on image points.

With the obtained $\widehat{\beta}_i^{(3)}$ $(i=1,2,\ldots,I)$, a similarity-invariant linear calibration algorithm (SILA) is designed as follows. In both the minimal configuration ($J=3$) and the redundant configurations ($J>3$), the constraint on ω is

$$\left(\widetilde{\mathbf{x}}_1-\widehat{\beta}_i^{(3)}\widetilde{\mathbf{x}}_J^i\right)^\top\omega\left(\widetilde{\mathbf{x}}_1-\widehat{\beta}_i^{(3)}\widetilde{\mathbf{x}}_J^i\right)=L_J^2. \tag{14}$$

Then, similar to (5), a linear system of equations on $\mathbf{w}$ can be obtained from constraints (14) as

$$\mathtt{V}\mathbf{w}=\mathbf{L}. \tag{15}$$

Then, $\widehat{\omega}$ and $\widehat{\mathtt{K}}$ are computed from $\widehat{\mathbf{w}}=\mathtt{V}^+\mathbf{L}$. The calibration result $\widehat{\mathtt{K}}$ in this algorithm is invariant under an image similarity normalization as proved in Section III-D. In the redundant configurations, the number of the constraints in (15) is smaller than that in (8), so the computational cost of SILA to obtain the least-squares solution is lower according to [17].

B. Accuracies of $\widehat{\beta}_i$ in the Minimal Configuration

Suppose the covariance matrix of the noises on image points has the diagonal form $\Sigma_{\mathbf{x}_1\mathbf{x}_2^i\mathbf{x}_3^i}=\mathrm{Diag}(\sigma_1^2,\sigma_1^2,\sigma_{2i}^2,\sigma_{2i}^2,\sigma_{3i}^2,\sigma_{3i}^2)$. Then, the standard deviation of $\widehat{\beta}_i$ can be approximated with

$$\mathrm{std}(\widehat{\beta}_i)\approx\left\|(\partial\widehat{\beta}_i)/(\partial\mathbf{x}_1\mathbf{x}_2^i\mathbf{x}_3^i)\right\|_{\Sigma_{\mathbf{x}_1\mathbf{x}_2^i\mathbf{x}_3^i}}$$

where the Jacobian $(\partial\widehat{\beta}_i)/(\partial\mathbf{x}_1\mathbf{x}_2^i\mathbf{x}_3^i)$ is calculated at the true values of image points [18].

When $J=3$, only one estimation of β_i is computed in (6) and it is represented by $\widehat{\beta}_i^{(2)}$. The normalization matrix used in FNLA can be written as

$$\mathtt{H}=\begin{pmatrix}s & 0 & s\,u_t\\ 0 & k\,s & k\,s\,v_t\\ 0 & 0 & 1\end{pmatrix} \tag{16}$$

where $[u_t,v_t]^\top$ is the translation vector, and s and $k\,s$ are the scaling factors [19]. We have the following proposition.

Proposition 1: $\mathrm{std}(\widehat{\beta}_i^{(2)})\geqslant\mathrm{std}(\widehat{\beta}_i^{(3)})$ for any normalization matrix $\mathtt{H}$.

Proof: The Jacobian of $\widehat{\beta}_i^{(2)}$ is

$$\frac{\partial\widehat{\beta}_i^{(2)}}{\partial\mathbf{x}_1\mathbf{x}_2^i\mathbf{x}_3^i}=\begin{pmatrix}\frac{L_3-L_2}{L_2}\\ \frac{L_2-L_3-\beta_iL_2}{L_2}\\ \beta_i\end{pmatrix}\otimes\mathtt{I}_{2\times3}\frac{[\widetilde{\mathbf{x}}_2^i]_\times\mathtt{H}^{*\top}\mathtt{H}^*(\widetilde{\mathbf{x}}_2^i\times\widetilde{\mathbf{x}}_3^i)}{\|\widetilde{\mathbf{x}}_2^i\times\widetilde{\mathbf{x}}_3^i\|^2_{\mathtt{H}^{*\top}\mathtt{H}^*}} \tag{17}$$

where the operator "$\otimes$" denotes the Kronecker product and $\mathtt{H}^*=\det(\mathtt{H})\mathtt{H}^{-\top}$. Then, $\mathrm{std}(\widehat{\beta}_i^{(2)})$ is approximated with

$$\begin{aligned}\mathrm{std}(\widehat{\beta}_i^{(2)})&\approx\left\|\frac{\partial\widehat{\beta}_i^{(2)}}{\partial\mathbf{x}_1\mathbf{x}_2^i\mathbf{x}_3^i}\right\|_{\Sigma_{\mathbf{x}_1\mathbf{x}_2^i\mathbf{x}_3^i}}\\&=\left\|\begin{pmatrix}\sigma_1\frac{L_3-L_2}{\beta_iL_2}\\ \sigma_{2i}\frac{L_2-L_3-\beta_iL_2}{\beta_iL_2}\\ \sigma_{3i}\end{pmatrix}\right\|\left\|\frac{\partial\widehat{\beta}_i^{(2)}}{\partial\mathbf{x}_3^i}\right\|.\end{aligned} \tag{18}$$

Similarly, the Jacobian of $\widehat{\beta}_i^{(3)}$ is

$$\frac{\partial\widehat{\beta}_i^{(3)}}{\partial\mathbf{x}_1\mathbf{x}_2^i\mathbf{x}_3^i}=\begin{pmatrix}\frac{L_3-L_2}{L_2}\\ \frac{L_2-L_3-\beta_iL_2}{L_2}\\ \beta_i\end{pmatrix}\otimes\frac{\mathbf{x}_2^i-\mathbf{x}_3^i}{\|\mathbf{x}_2^i-\mathbf{x}_3^i\|^2}. \tag{19}$$

$\mathrm{std}(\widehat{\beta}_i^{(3)})$ is approximated with

$$\begin{aligned}\mathrm{std}(\widehat{\beta}_i^{(3)})&\approx\left\|\frac{\partial\widehat{\beta}_i^{(3)}}{\partial\mathbf{x}_1\mathbf{x}_2^i\mathbf{x}_3^i}\right\|_{\Sigma_{\mathbf{x}_1\mathbf{x}_2^i\mathbf{x}_3^i}}\\&=\left\|\begin{pmatrix}\sigma_1\frac{L_3-L_2}{\beta_iL_2}\\ \sigma_{2i}\frac{L_2-L_3-\beta_iL_2}{\beta_iL_2}\\ \sigma_{3i}\end{pmatrix}\right\|\left\|\frac{\partial\widehat{\beta}_i^{(3)}}{\partial\mathbf{x}_3^i}\right\|.\end{aligned} \tag{20}$$

According to (18) and (20), $\mathrm{std}(\widehat{\beta}_i^{(2)})-\mathrm{std}(\widehat{\beta}_i^{(3)})$ has the same sign as $\left\|(\partial\widehat{\beta}_i^{(2)})/(\partial\mathbf{x}_3^i)\right\|-\left\|(\partial\widehat{\beta}_i^{(3)})/(\partial\mathbf{x}_3^i)\right\|$. Since $\left\|(\partial\widehat{\beta}_i^{(2)})/(\partial\mathbf{x}_3^i)\right\|\geqslant\left\|(\partial\widehat{\beta}_i^{(3)})/(\partial\mathbf{x}_3^i)\right\|$ as shown in (21) at the bottom of the next page, $\mathrm{std}(\widehat{\beta}_i^{(2)})\geqslant\mathrm{std}(\widehat{\beta}_i^{(3)})$ for any normalization matrix $\mathtt{H}$. ■

From Proposition 1 and its proof, some points can be revealed.

1) Since $\widehat{\beta}_i^{(1)}$ is a special case of $\widehat{\beta}_i^{(2)}$ when $\mathtt{H}=\mathtt{I}_{3\times3}$, $\widehat{\beta}_i^{(3)}$ is more accurate than $\widehat{\beta}_i^{(1)}$.
2) In real applications with high-resolution images, the scaling factors s and ks in FNLA are very small. Then, $\widehat{\beta}_i^{(2)}$ in FNLA

is close to the limit of $\widehat{\beta}_i^{(2)}$ as s approaches 0. Besides, by (21), we have

$$\lim_{s\to 0}\left\|\frac{\partial\widehat{\beta}_i^{(2)}}{\partial\mathbf{x}_3^i}\right\|^2-\left\|\frac{\partial\widehat{\beta}_i^{(3)}}{\partial\mathbf{x}_3^i}\right\|^2 = \frac{\beta_i^2(k^2-1)^2(u_2^i-u_3^i)^2(v_2^i-v_3^i)^2}{\left[\left(u_2^i-u_3^i\right)^2+\left(v_2^i-v_3^i\right)^2\right]\left[\left(u_2^i-u_3^i\right)^2+k^2\left(v_2^i-v_3^i\right)^2\right]^2}. \tag{22}$$

Then, when $k=1$, $\lim_{s\to 0}\|(\partial\widehat{\beta}_i^{(2)})/(\partial\mathbf{x}_3^i)\| = \|(\partial\widehat{\beta}_i^{(3)})/(\partial\mathbf{x}_3^i)\|$, when $k\neq 1$, $\lim_{s\to 0}\|(\partial\widehat{\beta}_i^{(2)})/(\partial\mathbf{x}_3^i)\| \geqslant \|(\partial\widehat{\beta}_i^{(3)})/(\partial\mathbf{x}_3^i)\|$. Therefore, according to (18) and (20), $\widehat{\beta}_i^{(2)}$ with isotropically scaled points will have similar accuracy to $\widehat{\beta}_i^{(3)}$, and the anisotropically scaled version of $\widehat{\beta}_i^{(2)}$ will have slightly worse accuracy.

C. Accuracies of $\widehat{\beta}_i$ in the Redundant Configurations

Suppose the J points on the 1-D object are uniformly fixed, i.e., $L_j=((j-1)/(J-1))L_J\,(j=2,...,J)$. Besides, the covariance matrix of the noises on image points is supposed to be $\sigma^2\mathtt{I}_{2J\times 2J}$.

The Accuracy of $\widehat{\beta}_{ij}^{(2)}$: Since the scaling factors of data normalization in FNLA are always small in real applications, each $\widehat{\beta}_{ij}^{(2)}$ is close to the limit of $\widehat{\beta}_{ij}^{(2)}$ as s approaches 0. Therefore, we only analyze this limit for the sake of convenience. With isotropic normalization, the Jacobian of $\widehat{\beta}_{ij}^{(2)}$ can be approximated with

$$\frac{\partial\widehat{\beta}_{ij}^{(2)}}{\partial\mathbf{x}_1\mathbf{x}_j^i\mathbf{x}_J^i}\approx\lim_{s\to 0}\frac{\partial\widehat{\beta}_{ij}^{(2)}}{\partial\mathbf{x}_1\mathbf{x}_j^i\mathbf{x}_J^i} = \begin{pmatrix}1+\frac{J-j}{\beta_i(j-1)}\\ -2-\frac{J-j}{\beta_i(j-1)}-\frac{\beta_i(j-1)}{J-j}\\ 1+\frac{\beta_i(j-1)}{J-j}\end{pmatrix}\otimes\frac{\beta_i(\mathbf{x}_1-\mathbf{x}_J^i)}{\|\mathbf{x}_1-\mathbf{x}_J^i\|^2}. \tag{23}$$

Then, $\mathrm{std}(\widehat{\beta}_{ij}^{(2)})\approx\sigma\|(\partial\widehat{\beta}_{ij}^{(2)})/(\partial\mathbf{x}_1\mathbf{x}_j^i\mathbf{x}_J^i)\|$ is an increasing function of $(J-j)/(\beta_i(j-1))+(\beta_i(j-1))/(J-j)$, and it is maximized at $j=2$ or $j=J-1$ for a given J. Furthermore, when $j=2$ or $j=J-1$, since β_i is usually close to 1, $(J-j)/(\beta_i(j-1))+(\beta_i(j-1))/(J-j)$ and $\mathrm{std}(\widehat{\beta}_{ij}^{(2)})$ increase with the increase of J. If $\widehat{\beta}_{ij}^{(2)}$ is computed with anisotropic normalization, the same conclusion still holds.

The Accuracy of $\widehat{\beta}_i^{(3)}$: The Jacobian of $\widehat{\beta}_i^{(3)}$ with respect to the image points is

$$\frac{\partial\widehat{\beta}_i^{(3)}}{\partial\mathbf{x}_j^i}=\frac{\alpha_{ij}}{\sum_{k=2}^{J-1}\frac{(k-1)^2(J-k)^2}{[J-k+\beta_i(k-1)]^2}}\frac{\mathbf{x}_1-\mathbf{x}_J^i}{\|\mathbf{x}_1-\mathbf{x}_J^i\|^2} \tag{24}$$

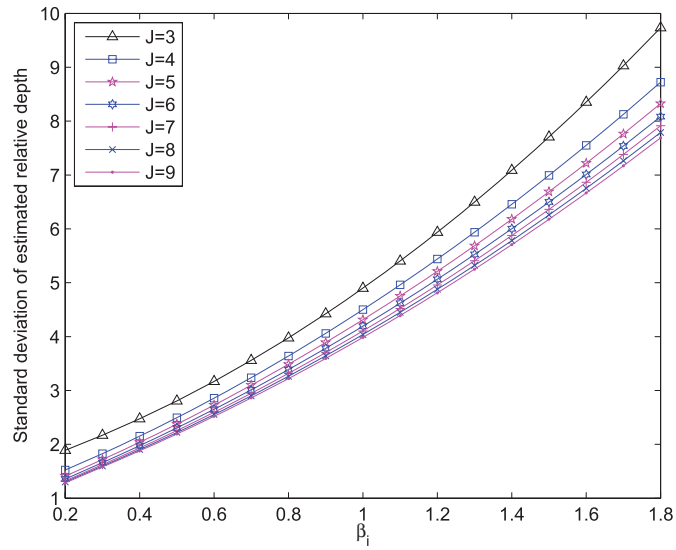

Fig. 2. Curves of $\|(\partial\widehat{\beta}_i^{(3)})/(\partial\mathbf{x}_1\mathbf{x}_{2..J}^i)\|\|\mathbf{x}_1-\mathbf{x}_J^i\|$ for $J=3,4,\ldots,9$.

where

$$\begin{aligned}\alpha_{i1}&=\sum_{k=2}^{J-1}\frac{(k-1)(J-k)^2}{J-k+\beta_i(k-1)}\\ \alpha_{ij}&=-(j-1)(J-j),\qquad j=2,\ldots,J-1\\ \alpha_{iJ}&=\sum_{k=2}^{J-1}\frac{\beta_i(k-1)^2(J-k)}{J-k+\beta_i(k-1)}.\end{aligned} \tag{25}$$

Then, the standard deviation of $\widehat{\beta}_i^{(3)}$ can be approximated with $\mathrm{std}(\widehat{\beta}_i^{(3)})\approx\sigma\|(\partial\widehat{\beta}_i^{(3)})/(\partial\mathbf{x}_1\mathbf{x}_{2..J}^i)\|$. Since σ and $\|\mathbf{x}_1-\mathbf{x}_J^i\|$ are unchanged when J varies, $\mathrm{std}(\widehat{\beta}_i^{(3)})$ is thus in proportion to $\|(\partial\widehat{\beta}_i^{(3)})/(\partial\mathbf{x}_1\mathbf{x}_{2..J}^i)\|\|\mathbf{x}_1-\mathbf{x}_J^i\|$, which is a function of β_i and J. For each value of J in $\{3,4,\ldots,9\}$, the curves of $\|(\partial\widehat{\beta}_i^{(3)})/(\partial\mathbf{x}_1\mathbf{x}_{2..J}^i)\|\|\mathbf{x}_1-\mathbf{x}_J^i\|$ are shown in Fig. 2. When J increases, the curve of $\|(\partial\widehat{\beta}_i^{(3)})/(\partial\mathbf{x}_1\mathbf{x}_{2..J}^i)\|\|\mathbf{x}_1-\mathbf{x}_J^i\|$ becomes lower, so $\mathrm{std}(\widehat{\beta}_i^{(3)})$ decreases with the increase of J.

To summarize the analyses of $\mathrm{std}(\widehat{\beta}_{ij}^{(2)})$ and $\mathrm{std}(\widehat{\beta}_i^{(3)})$, $\widehat{\beta}_i^{(3)}$ is more robust against noise than $\widehat{\beta}_{ij}^{(2)}$.

D. Influence of Data Normalization on the Calibration Accuracy

Although Francca *et al.* [6] considered that the calibration accuracy is improved in FNLA because data normalization decreases the condition number of the coefficient matrix, we reinvestigate the influence of data normalization on the calibration accuracy and provide a different explanation from that given in [6].

$$\begin{aligned}&\left\|\frac{\partial\widehat{\beta}_i^{(2)}}{\partial\mathbf{x}_3^i}\right\|^2-\left\|\frac{\partial\widehat{\beta}_i^{(3)}}{\partial\mathbf{x}_3^i}\right\|^2\\ &=\frac{\beta_i^2\left\{(k^2-1)(u_2^i-u_3^i)(v_2^i-v_3^i)+k^2s^2\left[(u_2^i+u_t)(v_3^i+v_t)-(v_2^i+v_t)(u_3^i+u_t)\right]\left[(u_2^i+u_t)(u_2^i-u_3^i)+(v_2^i+v_t)(v_2^i-v_3^i)\right]\right\}^2}{\left[(u_2^i-u_3^i)^2+(v_2^i-v_3^i)^2\right]\left\{(u_2^i-u_3^i)^2+k^2(v_2^i-v_3^i)^2+k^2s^2[(u_2^i+u_t)(v_3^i+v_t)-(v_2^i+v_t)(u_3^i+u_t)]^2\right\}^2}\\ &\geqslant 0\end{aligned} \tag{21}$$

To test the influence of the condition number on the calibration accuracy, we assume that the estimations of the relative depths are identical in ZLA and FNLA, i.e., $\widehat{\beta}_i^{(1)} = \widehat{\beta}_i^{(2)}$ $(i = 1, 2, \ldots, I)$. Then, Hartley's method to analyze the influence of data normalization on the eight-point algorithm in [19] is utilized as follows. It can be verified that there exists an invertible 6×6 matrix $\mathtt{S}$ such that $\mathtt{V}' = \mathtt{VS}$ and $\mathbf{w}' = \mathtt{S}^{-1}\mathbf{w}$ if and only if $\omega' = \mathtt{H}^{-\top}\omega\mathtt{H}^{-1}$. Thus $\omega' = \mathtt{H}^{-\top}\omega\mathtt{H}^{-1}$ is the one-to-one correspondence between ω and ω' such that $\mathtt{V}\mathbf{w} - \mathbf{L} = \mathtt{V}'\mathbf{w}' - \mathbf{L}$. Then, the least-squares solutions to (5) and (8) are related by $\widehat{\omega}' = \mathtt{H}^{-\top}\widehat{\omega}\mathtt{H}^{-1}$. As a result, the retrieved estimation of the IAC in FNLA is the same as that in ZLA, since $\widehat{\omega} = \mathtt{H}^{\top}\widehat{\omega}'\mathtt{H}$.

The above deduction shows that, if $\widehat{\beta}_i$ $(i = 1, 2, \ldots, I)$ are invariant to $\mathtt{H}$, the calibration result $\widehat{\mathtt{K}}$ is also invariant regardless of the condition numbers of $\mathtt{V}$ and $\mathtt{V}'$. Then, we speculate that the improved accuracy of FNLA over ZLA is because $\widehat{\beta}_i^{(2)}$ $(i = 1, 2, \ldots, I)$ are more accurate than $\widehat{\beta}_i^{(1)}$.

Next, we consider the influence of data normalization on the accuracy of SILA. Since $\widehat{\beta}_i^{(3)}$ $(i = 1, 2, \ldots, I)$ in SILA are invariant to similarity transform (isotropic normalization), the calibration result of SILA is also similarity-invariant. Thus, the calibration accuracy of SILA cannot be improved through isotropic normalization. Besides, similar to the influence of anisotropic normalization on the accuracy of $\widehat{\beta}_i^{(2)}$, anisotropic normalization will reduce the accuracy of $\widehat{\beta}_i^{(3)}$, resulting in declined accuracy of SILA. To summarize the discussions on the influences of isotropic normalization and anisotropic normalization, SILA does not need data normalization.

IV. Weighted Similarity-Invariant Linear Algorithm (WSILA)

Since the estimated relative depths $\widehat{\beta}_i^{(3)}$ in different poses have different accuracies, the constraints on the IAC including these $\widehat{\beta}_i^{(3)}$ have different levels of importance. Therefore, a weighed similarity-invariant linear calibration algorithm is proposed based on SILA, where each constraint is weighted with the reciprocal of the standard deviation of corresponding $\widehat{\beta}_i^{(3)}$.

From Fig. 2, we see that $\left\|(\partial\widehat{\beta}_i^{(3)})/(\partial\mathbf{x}_1\mathbf{x}_{2..J}^i)\right\| \approx k_J(\beta_i{}^2)/(\|\mathbf{x}_1 - \mathbf{x}_J^i\|)$, where k_J is a constant related to J. Suppose the covariance matrix of the noises on image points is $\sigma^2\mathtt{I}_{2J\times 2J}$, and then

$$\mathrm{std}(\widehat{\beta}_i^{(3)}) \approx \sigma\left\|\frac{\partial\widehat{\beta}_i^{(3)}}{\partial\mathbf{x}_1\mathbf{x}_{2..J}^i}\right\| \approx k_J\sigma\frac{\beta_i^2}{\|\mathbf{x}_1 - \mathbf{x}_J^i\|}. \tag{26}$$

Since k_J and σ are both constant for different i, the weight on the constraint corresponding to the pose i is defined as

$$w_i = \frac{1}{\mathrm{std}(\widehat{\beta}_i^{(3)})} \approx \frac{\|\mathbf{x}_1 - \mathbf{x}_J^i\|}{\widehat{\beta}_i^{(3)2}}. \tag{27}$$

Define the weighting matrix $\mathtt{W} = \mathrm{Diag}(w_1, w_2, \ldots, w_I)$. Then, the weighted linear system is

$$\mathtt{WV}\mathbf{w} = \mathtt{W}\mathbf{L} \tag{28}$$

where the constructions of $\mathtt{V}$ and $\mathbf{L}$ are the same as in SILA. Then, $\widehat{\omega}$ and $\widehat{\mathtt{K}}$ can be computed from $\widehat{\mathbf{w}} = (\mathtt{WV})^{+}\mathtt{W}\mathbf{L}$. The computational load of this weighted linear algorithm is nearly the same as that of SILA, since it is easy to compute such weights.

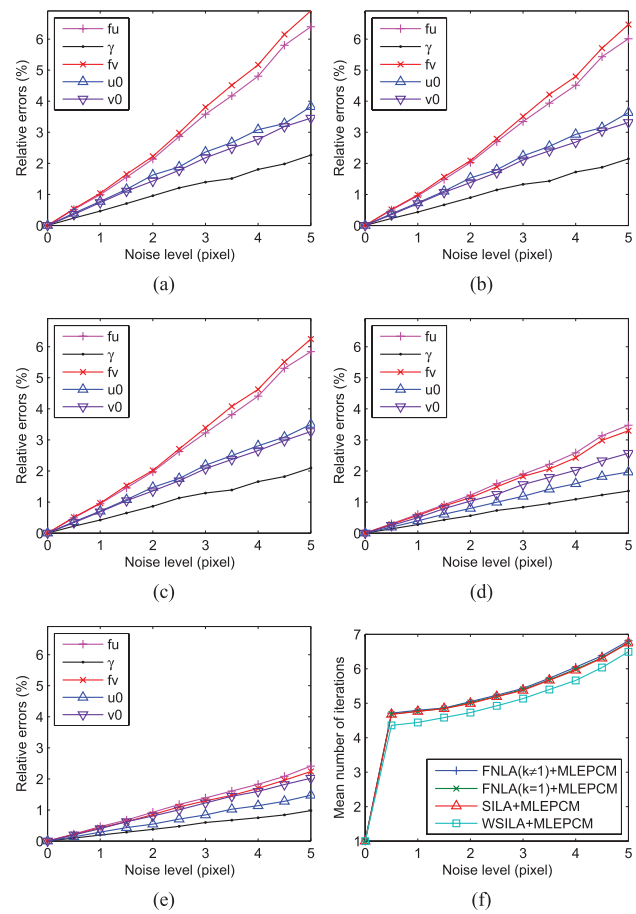

Fig. 3. Calibration errors in the minimal configuration. (a) Anisotropic FNLA. (b) Isotropic FNLA. (c) SILA. (d) WSILA. (e) WSILA + MLEPCM. (f) Average iteration numbers of MLEPCM with different initial values.

V. Experimental Results

A. Synthetic Data

In the synthetic experiments, the camera intrinsic parameters are $f_u = 3150$, $f_v = 3250$, $\gamma = 3$, $u_0 = 1504$, $v_0 = 1000$, and the image resolution is 3008×2000 pixels. The length of the 1-D object is 60, and the fixed point is $\mathbf{X}_1 = [0, -25, 150]^{\top}$. The spherical coordinates parameters θ and ϕ of 30 poses of the 1-D object are randomly chosen from the distributions $\theta \sim \mathrm{Uniform}(0.2\pi, 0.8\pi)$ and $\phi \sim \mathrm{Uniform}(0, \pi)$. Independent and identically distributed Gaussian noises are added to the projections of points on the 1-D object. In each set of the following experiments, the calibration procedure is repeated 1000 times. Then, we report the relative errors of different 1-D calibration algorithms as in [20], where the relative errors are the ratios of the root-mean-square errors of the estimated intrinsic parameters to the ground truth of f_u.

1) Calibration Accuracy in the Minimal Configuration: Here, three equidistant collinear points are fixed on the 1-D object. The standard deviation of zero-mean Gaussian noise varies from 0 to 5 pixels with a step of 0.5 pixel. The calibration accuracies of FNLA with anisotropic normalization, FNLA with isotropic normalization, SILA, WSILA, and MLEPCM are shown in Fig. 3.

As seen in Fig. 3(a)–(d), the calibration accuracies of FNLA with anisotropic normalization and isotropic normalization and SILA are similar but the accuracy of WSILA is much higher than both of them. When the results of these four linear calibration algorithms are used

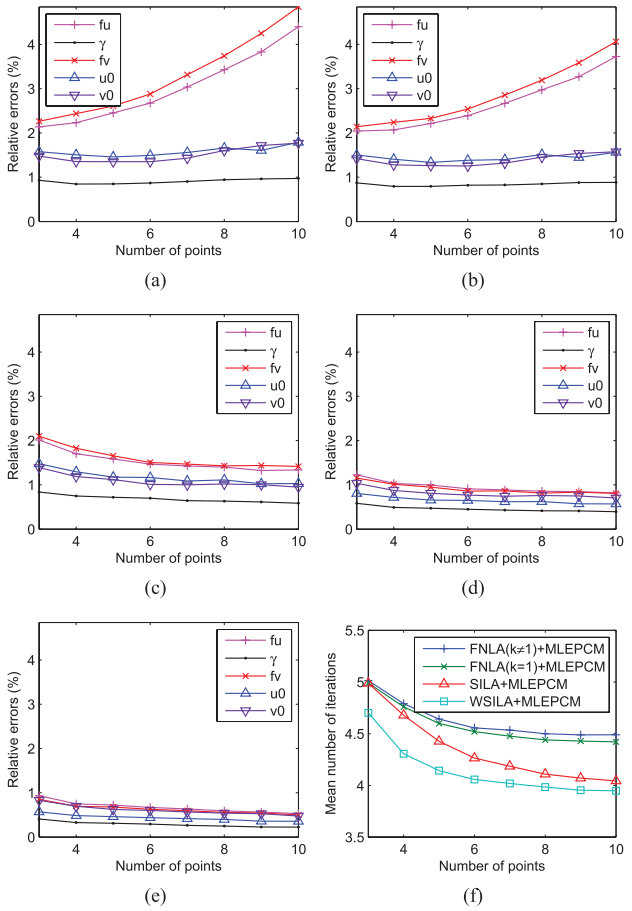

Fig. 4. Calibration errors in the redundant configurations. (a) Anisotropic FNLA. (b) Isotropic FNLA. (c) SILA. (d) WSILA. (e) WSILA + MLEPCM. (f) Average iteration numbers of MLEPCM with different initial values.

as the initialization of MLEPCM, the differences between the relative errors of the four refined results are smaller than 0.002%. Hence, only the accuracy of MLEPCM initialized with WSILA is shown in Fig. 3(e), which is slightly higher than that of WSILA. Fig. 3(f) shows that, when the results of WSILA are used as the initial values, the least number of iterations is required by MLEPCM.

2) Calibration Accuracy in the Redundant Configurations: Here, more than three points are uniformly fixed on the 1-D object. The standard deviation of zero-mean Gaussian noise is 2 pixels. We vary J from 3 to 10 with a step of 1. The accuracies of FNLA with anisotropic normalization, FNLA with isotropic normalization, SILA, WSILA, and MLEPCM for different values of J are shown in Fig. 4.

As seen in Fig. 4(a) and (b), the errors of FNLA with anisotropic normalization and isotropic normalization become larger with the increase of J. However, the accuracy of SILA becomes higher with the increase of J, and WSILA is more accurate than SILA as shown in Fig. 4(c) and (d). When the results of these four linear algorithms are used as the initialization of MLEPCM, the differences between the relative errors of the four refined results are smaller than 10^{-5}%, so only the accuracy of MLEPCM initialized with WSILA is shown in Fig. 4(e). WSILA has the closest accuracy to MLEPCM among the linear calibration algorithms. As seen in Fig. 4(f), when the results of WSILA are used as the initial values, the least number of iterations is required by MLEPCM.

B. Real Image Data

In the experiments on real image data, seven ping-pong balls are fixed on a metal stick that rotates around a ball at the end.

Fig. 5. Images of calibration objects. (a) 1-D object. (b) Checkerboard.

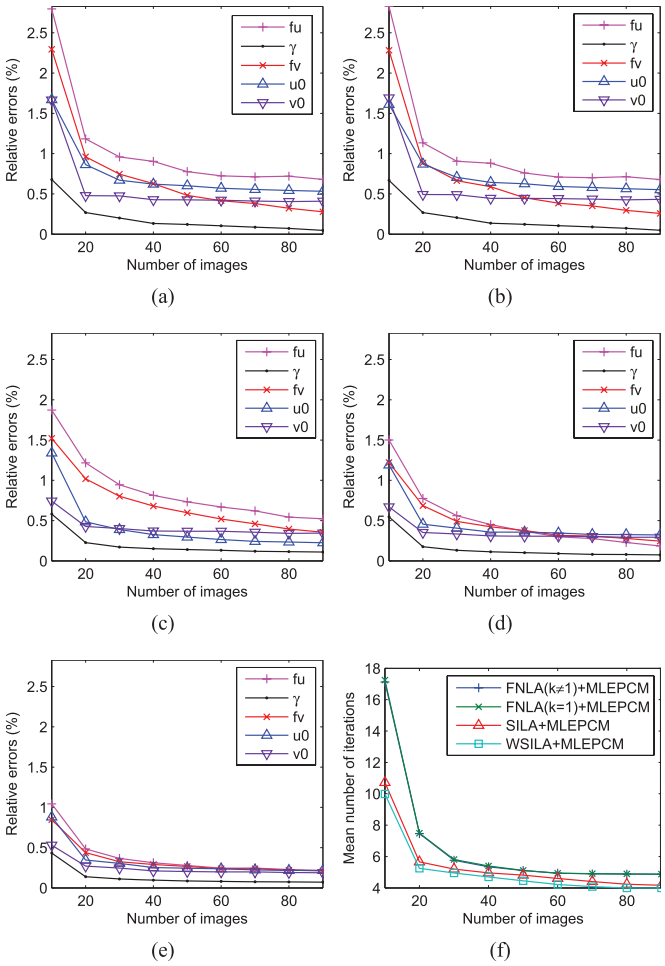

Fig. 6. Calibration errors concerning the number of images. (a) Anisotropic FNLA. (b) Isotropic FNLA. (c) SILA. (d) WSILA. (e) WSILA + MLEPCM. (f) Average iteration numbers of MLEPCM with different initializations.

The distances between the center of the fixed ball and the centers of other six balls are $[L_2, L_3, L_4, L_5, L_6, L_7] = [9.999, 19.968, 29.966, 39.905, 49.887, 59.861]$ cm. When the stick rotates, 112 images are captured with a camera of resolution 3008 $\times$ 2000 pixels. In each image, the centers of seven ellipses are used as the projections of balls' centers. Then, FNLA with anisotropic normalization, FNLA with isotropic normalization, SILA, WSILA, and MLEPCM are used to calibrate the camera. And the result of the planar calibration algorithm [14], [21] is used as the benchmark, where 82 images of a checkerboard are captured. The sample images of the 1-D object and the checkerboard are shown in Fig. 5.

To evaluate the calibration accuracy concerning the number of images I, we vary I from 10 to 90 with a step of 10. And for each value of I, 250 trials of 1-D calibration procedures are executed after

randomly choosing I images from the total available set. We report the relative errors in Fig. 6. Here, when the results of the four linear algorithms are used as the initializations of MLEPCM, the differences between the relative errors of the four refined results are smaller than 0.04% when $I = 10$, and smaller than $10^{-5}\%$ when $I \geqslant 20$. Thus, only the accuracy of MLEPCM initialized with the results of WSILA is shown.

It is seen from Fig. 6(a)–(e) that the errors of FNLA with anisotropic normalization, FNLA with isotropic normalization, SILA, and WSILA are approximately 2.4, 2.4, 2.0, and 1.4 times that of MLEPCM respectively, which shows that WSILA has higher accuracy than unweighted linear algorithms. Moreover, when the results of WSILA are used as the initial values of MLEPCM, the least iteration number is required as shown in Fig. 6(f).

It has to be pointed out that in the real data experiments, the centers of the apparent contour ellipses generally do not coincide with the projections of the balls' centers $\mathbf{x}_j^i$ [22], which may introduce biases in the measurements of $\mathbf{x}_j^i$. To solve this problem, we can first calibrate the camera with the biased measurements of $\mathbf{x}_j^i$, and then refine $\mathbf{x}_j^i$ with the obtained intrinsic parameters [22]. With these refined estimations of $\mathbf{x}_j^i$, more accurate camera parameters can be obtained by calibrating the camera once again. As for our real data experiments, we found that the differences between the refined estimations of $\mathbf{x}_j^i$ and the centers of the ellipses were so small that the calibration accuracy improved only very slightly, and therefore we did not calibrate the camera twice here.

VI. Conclusion

This paper proposed a weighted similarity-invariant linear 1-D calibration algorithm that can achieve sufficient accuracy at low computational complexity. In addition, it can provide a good initial value for the maximum-likelihood method if higher accuracy is required. A number of experimental results demonstrated the effectiveness of the proposed algorithm.

The main contributions of this paper include the following. 1) A new algorithm to estimate the relative depth is proposed, which is more robust against noise than existing algorithms. 2) A new explanation is provided as to why the accuracy of FNLA [6] is higher than that of ZLA [1]. 3) The accuracy of the proposed WSILA can be improved further when more points are fixed on the 1-D object.

References

[1] Z. Zhang, "Camera calibration with one-dimensional objects," *IEEE Trans. Pattern Anal. Mach. Intell.*, vol. 26, no. 7, pp. 892–899, Jul. 2004.

[2] F. Wu, Z. Hu, and H. Zhu, "Camera calibration with moving one-dimensional objects," *Pattern Recognit.*, vol. 38, pp. 755–765, May 2005.

[3] P. Hammarstedt, P. Sturm, and A. Heyden, "Degenerate cases and closed-form solutions for camera calibration with one-dimensional objects," in *Proc. IEEE Int. Conf. Comput. Vis.*, vol. 1. Oct. 2005, pp. 317–324.

[4] F. Qi, Q. Li, Y. Luo, and D. Hu, "Camera calibration with one-dimensional objects moving under gravity," *Pattern Recognit.*, vol. 40, no. 1, pp. 343–345, 2007.

[5] F. Qi, Q. Li, Y. Luo, and D. Hu, "Constraints on general motions for camera calibration with one-dimensional objects," *Pattern Recognit.*, vol. 40, no. 6, pp. 1785–1792, 2007.

[6] J. A. de Francca, M. R. Stemmer, M. B. de M. Francca, and E. G. Alves, "Revisiting Zhang's 1D calibration algorithm," *Pattern Recognit.*, vol. 43, no. 3, pp. 1180–1187, 2010.

[7] L. Wang, F. Duan, and C. Liang, "A global optimal algorithm for camera calibration with one-dimensional objects," in *Proc. 14th Int. Conf. Human-Comput. Interact., Des. Dev. Appr.*, 2011, pp. 660–669.

[8] I. Miyagawa, H. Arai, and H. Koike, "Simple camera calibration from a single image using five points on two orthogonal 1-D objects," *IEEE Trans. Image Process.*, vol. 19, no. 6, pp. 1528–1538, Jun. 2010.

[9] L. Wang, F. Wu, and Z. Hu, "Multi-camera calibration with one-dimensional object under general motions," in *Proc. IEEE Int. Conf. Comput. Vis.*, Oct. 2007, pp. 1–7.

[10] H. Lei, Z. Wei, and G. Zhang, "A simple global calibration method based on 1D target for multi-binocular vision sensor," in *Proc. Int. Symp. Comput. Sci. Comput. Technol.*, vol. 2. 2008, pp. 290–294.

[11] Z. Liu, G. Zhang, Z. Wei, and J. Sun, "Novel calibration method for non-overlapping multiple vision sensors based on 1D target," *Opt. Lasers Eng.*, vol. 49, no. 4, pp. 570–577, 2011.

[12] L. Davis, E. Borovikov, R. Cutler, D. Harwood, and T. Horprasert, "Multi-perspective analysis of human action," in *Proc. Int. Workshop Cooperat. Distrib. Vis.*, 1999, pp. 1–37.

[13] C. Zitnick, S. Kang, M. Uyttendaele, S. Winder, and R. Szeliski, "High-quality video view interpolation using a layered representation," *ACM SIGGRAPH*, vol. 23, no. 3, pp. 600–608, 2004.

[14] Z. Zhang, "A flexible new technique for camera calibration," *IEEE Trans. Pattern Anal. Mach. Intell.*, vol. 22, no. 11, pp. 1330–1334, Nov. 2000.

[15] R. Tsai, "A versatile camera calibration technique for high-accuracy 3D machine vision metrology using off-the-shelf TV cameras and lenses," *IEEE J. Robot. Autom.*, vol. 3, no. 4, pp. 323–344, Aug. 1987.

[16] J. Heikkilä, "Geometric camera calibration using circular control points," *IEEE Trans. Pattern Anal. Mach. Intell.*, vol. 22, no. 10, pp. 1066–1077, Oct. 2000.

[17] G. Golub and C. Van Loan, *Matrix Computations*. Baltimore, MD: Johns Hopkins Univ., 1996, p. 694.

[18] J. C. Clarke, "Modelling uncertainty: A primer," Dept. Eng. Sci., University Oxford, Oxford, U.K., Tech. Rep. 2161/98, 1998.

[19] R. I. Hartley, "In defense of the eight-point algorithm," *IEEE Trans. Pattern Anal. Mach. Intell.*, vol. 19, no. 6, pp. 580–593, Jun. 1997.

[20] B. Triggs, "Autocalibration from planar scenes," in *Proc. Eur. Conf. Comput. Vis.*, 1998, pp. 89–105.

[21] J.-Y. Bouguet. (2010, Jul. 9). *Camera Calibration Toolbox for MATLAB* [Online]. Available: http://www.vision.caltech.edu/bouguetj/calib_doc/

[22] K.-Y. K. Wong, D. Schnieders, and S. Li, "Recovering light directions and camera poses from a single sphere," in *Proc. Eur. Conf. Comput. Vis.*, 2008, pp. 631–642.